

Non-axisymmetric instability of centrifugally stable stratified Taylor–Couette flow

By IRAD YAVNEH¹, JAMES C. McWILLIAMS²
AND M. JEROEN MOLEMAKER²

¹Department of Computer Science, Technion, Haifa 3200, Israel

²IGPP, University of California at Los Angeles, Los Angeles, CA 90095-1567, USA

(Received 2 February 2000 and in revised form 3 February 2001)

The stability is investigated of the swirling flow between two concentric cylinders in the presence of stable axial linear density stratification, for flows not satisfying the well-known Rayleigh criterion for inviscid centrifugal instability, $d(Vr)^2/dr < 0$. We show by a linear stability analysis that a sufficient condition for non-axisymmetric instability is, in fact, $d(V/r)^2/dr < 0$, which implies a far wider range of instability than previously identified. The most unstable modes are radially smooth and occur for a narrow range of vertical wavenumbers. The growth rate is nearly independent of the stratification when the latter is strong, but it is proportional to it when it is weak, implying stability for an unstratified flow. The instability depends strongly on a non-dimensional parameter, S , which represents the ratio between the strain rate and twice the angular velocity of the flow. The instabilities occur for anti-cyclonic flow ($S < 0$). The optimal growth rate of the fastest-growing mode, which is non-oscillatory in time, decays exponentially fast as S (which can also be considered a Rossby number) tends to 0. The mechanism of the instability is an arrest and phase-locking of Kelvin waves along the boundaries by the mean shear flow. Additionally, we identify a family of (probably infinitely many) unstable modes with more oscillatory radial structure and slower growth rates than the primary instability. We determine numerically that the instabilities persist for finite viscosity, and the unstable modes remain similar to the inviscid modes outside boundary layers along the cylinder walls. Furthermore, the nonlinear dynamics of the anti-cyclonic flow are dominated by the linear instability for a substantial range of Reynolds numbers.

1. Introduction

Fluid flow in an annulus between concentric rotating cylinders—generally known as circular Couette or Taylor–Couette flow (Couette 1890; Taylor 1923)—is a classical problem of hydrodynamic stability, and it has served as an important paradigm for the dynamics of sheared flows. Many theoretical and experimental studies of this problem have been made for fluids with uniform density (e.g. the classic treatise of Chandrasekhar 1961; the experimental study of Andereck, Liu & Swinney 1986; and the survey of Tagg 1994).

One might reasonably guess that this flow regime has become well understood, but here we report on a qualitatively different type of instability. We examine Taylor–Couette flow with a stable axial density stratification. This problem was first studied by Thorpe (1966), who mainly investigated the analogy of the stratified Taylor–Couette problem with the problem of rotating Bénard convection. No further studies on this

problem were published until the work of Boubnov, Gledzer & Hopfinger (1995), who investigated experimentally and theoretically (by a linear stability theory) the case where the outer cylinder is at rest and only the inner cylinder is rotating. Their main conclusions are that the stratification has a stabilizing effect on the flow, with the critical Reynolds number for the onset of instability increasing with the strength of stratification. The unstable mode is non-axisymmetric and oscillatory in time. The stratification reduces the vertical wavelength of the most amplified modes at the onset of instability. Hua, Le Gentil & Orlandi (1997) made an extensive numerical study of this problem for conditions similar to the experiments of Boubnov *et al.* (1995) and reproduce the main features seen in the experiments. They show that the main effect of the axial stratification is a reduction of the height of the so-called Taylor vortices and the formation of density layers of small vertical-to-horizontal aspect ratio. They also show that the initial instability is axisymmetric, while non-axisymmetric motions appear only at a slightly higher Reynolds number than the critical one. Further studies of this problem are reported in Boubnov *et al.* (1996), Boubnov & Hopfinger (1997), and Caton, Janiaud & Hopfinger (1999).

A common feature to all the stratified studies (except Thorpe 1966) is that the outer cylinder is at rest. Recall the famous criterion for axisymmetric instability of an inviscid fluid, due to Rayleigh (1916) and extended to stratified fluids and a baroclinic circular vortex by Ooyama (1966):

$$\frac{d(Vr)^2}{dr} < 0, \quad (1)$$

where V is the (azimuthal) velocity. When the outer cylinder is at rest, this condition is obviously satisfied for any rotation rate of the inner cylinder. Indeed, Boubnov *et al.* (1995) give an analytical solution for the inviscid limit with axisymmetric perturbations about the mean Taylor–Couette flow. They note that this flow is always unstable for sufficiently large vertical wavenumbers.

In addition to the importance of stratified Taylor–Couette as a realizable laboratory flow, it also has value as a canonical example of the interplay between (planetary) rotation, stable density stratification, velocity shear, and horizontal boundaries—all of which are common ingredients for the large-scale, geophysical fluid dynamics in the Earth’s ocean and atmosphere. We show below new modes of instability that are clearly distinct from the more familiar barotropic, baroclinic, centrifugal/inertial, and convective instabilities that can also arise from these ingredients. Furthermore, the new instabilities are most important for intermediate values of the Rossby number, which is a regime of particular interest since it coincides with the breakdown of the quasi-static, geostrophic or gradient-wind, horizontal force balances that are pervasive in large-scale geophysical flows (McWilliams *et al.* 1998).

Here we study stably stratified Taylor–Couette flow which is centrifugally stable (i.e. does not satisfy (1)). No linear instabilities are known to exist in this regime in the classical (unstratified) Taylor–Couette flow (e.g. Tagg 1994). The governing equations are given in §2. In §3 we derive an upper bound on the growth rate and then perform a linear stability analysis. We show that, in the inviscid limit, the stratified Taylor–Couette flow is unstable if the angular velocity of the outer cylinder is smaller in magnitude than that of the inner cylinder. The optimal growth rates are substantial (compared to the upper bound) when the flow is nearly irrotational, but they decay exponentially fast as the relative rotation rate is increased. Section 4 describes the mechanism of the instability, which is analogous to that studied by Kushner, McIntyre & Shepherd (1998) for rotating, stratified, channel flow, and

earlier by Satomura (1981a) for nonrotating stratified shallow-water channel flow. In §5 we present numerical results, including an apparently infinite family of more weakly unstable modes. We also examine the effects of a small viscosity and in §6 briefly discuss the significance of the linear instability in a realizable laboratory environment. Concluding remarks are in §7.

2. Governing equations

In cylindrical coordinates the Boussinesq equations for incompressible stratified flow with uniform viscosity are

$$U_t + (\mathbf{U} \cdot \nabla)U - \frac{V^2}{r} = -\frac{1}{\bar{\rho}_0}P_r + \nu \left(\Delta U - \frac{U}{r^2} - \frac{2V_\theta}{r^2} \right), \quad (2)$$

$$V_t + (\mathbf{U} \cdot \nabla)V + \frac{UV}{r} = -\frac{1}{\bar{\rho}_0 r}P_\theta + \nu \left(\Delta V - \frac{V}{r^2} + \frac{2U_\theta}{r^2} \right), \quad (3)$$

$$W_t + (\mathbf{U} \cdot \nabla)W + g \frac{\rho^*}{\bar{\rho}_0} = -\frac{1}{\bar{\rho}_0}P_z + \nu \Delta W, \quad (4)$$

$$\rho^* + (\mathbf{U} \cdot \nabla)\rho^* + W \frac{d\rho_0}{dz} = 0, \quad (5)$$

$$\frac{1}{r}(rU)_r + \frac{1}{r}V_\theta + W_z = 0, \quad (6)$$

where (U, V, W) are the components of velocity in directions (r, θ, z) , respectively, and the density is decomposed into the background stratification and perturbations about it, $\rho(r, \theta, z, t) = \bar{\rho}_0(z) + \rho^*(r, \theta, z, t)$. For simplicity, the density diffusion term has been neglected, since its action occurs only on times longer than the dynamical events of interest here. We assume throughout this paper that the stable density stratification is linear, so that the Brunt–Väisälä frequency (squared), $N^2 = -(g/\bar{\rho}_0)(d\rho_0/dz)$, is constant.

The steady axisymmetric solution of (2)–(6) for the Taylor–Couette problem is $V = Ar + B/r$, $U = W = 0$, with $A = [r_0 V(r_0) - r_1 V(r_1)]/(r_0^2 - r_1^2)$, and $B = [r_1 V(r_0) - r_0 V(r_1)]r_0 r_1/(r_1^2 - r_0^2)$, where r_0 and r_1 denote the radii of the inner and outer cylinders, respectively.

3. Linear stability analysis

Let $\Omega = V/r$ denote the angular velocity of the steady flow. The vorticity associated with the flow is denoted $Z = (1/r)(d/dr)(rV)$. For the Taylor–Couette steady solution, $\Omega = A + B/r^2$, and $Z = 2A$, but we first derive the general linearized equations for axisymmetric barotropic mean flow and later apply them to this special case.

3.1. Linearized equations

We linearize (2)–(6) around the steady solution and obtain the equations for small perturbations, $(\hat{u}, \hat{v}, \hat{w}, \hat{p} = P\bar{\rho}_0^{-1}, \hat{h} = -(d\rho_0/dz)^{-1}\rho^*)$. Here, \hat{h} is the perturbation in the vertical displacement. The linearized equations are

$$D\hat{u} - 2\Omega\hat{v} = -\hat{p}_r + \nu \left(\Delta\hat{u} - \frac{\hat{u}}{r^2} - \frac{2\hat{v}_\theta}{r^2} \right), \quad (7)$$

$$D\hat{v} + Z\hat{u} = -\frac{1}{r}\hat{p}_\theta + v \left(\Delta\hat{v} - \frac{\hat{v}}{r^2} + \frac{2\hat{u}_\theta}{r^2} \right), \quad (8)$$

$$D\hat{w} + N^2\hat{h} = -\hat{p}_z + v\Delta\hat{w}, \quad (9)$$

$$D\hat{h} = \hat{w}, \quad (10)$$

$$\frac{1}{r}(r\hat{u})_r + \frac{1}{r}\hat{v}_\theta + \hat{w}_z = 0, \quad (11)$$

where $D = \partial_t + \Omega\partial_\theta$ is the material derivative. The boundary conditions at the cylinder walls are $(\hat{u}, \hat{v}, \hat{w}) = 0$. We consider a domain that is infinite in the vertical direction, and periodicity is assumed.

We restrict our analysis to the inviscid equations, $v = 0$, with no-normal-flow conditions at the walls, $u = 0$. Viscous effects are tested in §5.4. Buoyancy diffusion is neglected.

3.1.1. Energy equation and an upper bound on the growth rate

An equation can be written for the energy of the perturbations. It yields an upper bound on their growth rate, and so provides a scale for the strength of instabilities. We define the inner product of two real-valued functions f and g by

$$\langle f, g \rangle = \int_V fg \, d\mathbf{v}, \quad (12)$$

where V denotes an annular domain whose vertical extent is some integer number of periods. The associated L_2 norm is defined by $\|f\|_2 = \langle f, f \rangle^{1/2}$. Define the (kinetic plus potential) energy of the perturbations by

$$E = \frac{1}{2}(\|\hat{u}\|_2^2 + \|\hat{v}\|_2^2 + \|\hat{w}\|_2^2 + N^2\|\hat{h}\|_2^2). \quad (13)$$

If we take the inner products of (7)–(10) with \hat{u} , \hat{v} , \hat{w} and $N^2\hat{h}$, respectively, and sum up the terms, we obtain

$$E_t + \langle (Z - 2\Omega)\hat{u}, \hat{v} \rangle = -(\langle \hat{u}, \hat{p}_r \rangle + \langle \hat{v}, (1/r)\hat{p}_\theta \rangle + \langle \hat{w}, \hat{p}_z \rangle), \quad (14)$$

where the azimuthal advection terms vanish due to the periodicity and the axisymmetry of Ω . Integration by parts of the right-hand side of (14) yields $\langle \nabla \cdot \hat{\mathbf{u}}, \hat{\mathbf{p}} \rangle$, where $\hat{\mathbf{u}} = (\hat{u}, \hat{v}, \hat{w})$, and all boundary terms vanish due to the periodicity and boundary conditions. Thus, the right-hand side vanishes by (11). We define the strain rate of the mean flow by

$$\mathcal{S} = r\Omega' = Z - 2\Omega, \quad (15)$$

and rewrite the energy equation as

$$E_t = -\langle \mathcal{S}\hat{u}, \hat{v} \rangle. \quad (16)$$

Equation (16) provides an upper bound on the growth rate of E . Using

$$0 \leq \frac{1}{2}\|\hat{u} \pm \hat{v}\|_2^2 = \frac{1}{2}(\|\hat{u}\|_2^2 + \|\hat{v}\|_2^2) \pm \langle \hat{u}, \hat{v} \rangle \leq E \pm \langle \hat{u}, \hat{v} \rangle, \quad (17)$$

we obtain by (16) $E_t \leq \|\mathcal{S}\|_\infty \langle \hat{u}, \hat{v} \rangle \leq \|\mathcal{S}\|_\infty E$, where $\|\cdot\|_\infty$ denotes the maximum norm, so that for Taylor–Couette flow $\|\mathcal{S}\|_\infty = 2|B|/r_0^2$. This yields

$$E \leq E_0 \exp(\|\mathcal{S}\|_\infty t), \quad (18)$$

where E_0 is the energy at some initial time $t = 0$.

3.2. Normal-mode form

Assume the perturbations to be of the normal-mode form,

$$(\hat{u}, \hat{v}, \hat{w}, \hat{p}, \hat{h})(r, \theta, z, t) = (u, v, w, p, h)(r)e^{i(\ell\theta + mz - \omega t)}. \quad (19)$$

Here, ℓ and m are the azimuthal and vertical wavenumbers, respectively, and $\omega = \omega_r + i\omega_i$, where ω_r represents the frequency of the perturbation oscillations and ω_i is the growth rate. For the domain we are considering, m may be any real number, but ℓ can only take on integer values. Nevertheless, we treat ℓ as a real number in the derivations, and only refer to its being an integer when such a distinction becomes important.

The linearized inviscid equations are

$$-i\sigma u - 2\Omega v = -p', \quad (20)$$

$$-i\sigma v + Z u = -\frac{i\ell}{r} p, \quad (21)$$

$$-i\sigma w + N^2 h = -i m p, \quad (22)$$

$$-i\sigma h = w, \quad (23)$$

$$\frac{1}{r}(ru)' + \frac{i\ell}{r} v + i m w = 0, \quad (24)$$

where primes denote derivatives with respect to r , and $\sigma = \omega - \ell\Omega(r)$. From (20)–(24) we derive a single equation for u , the perturbation in the radial velocity (see Appendix A),

$$[G(N^2 - \sigma^2)r(ru)']' + \left\{ \frac{\ell}{\sigma} [G(N^2 - \sigma^2)Z]' - 2G\Omega Z r m^2 - \frac{1}{r} \right\} (ru) = 0, \quad (25)$$

with $G(r) = [\ell^2(N^2 - \sigma^2) - r^2 m^2 \sigma^2]^{-1}$. As we are only interested in unstable modes, we assume throughout that ω_i is non-zero. Also, the case $\ell = m = 0$ is excluded because (24) and the boundary conditions then imply $u = 0$. Hence, G is bounded.

3.3. Non-dimensionalization and scaling

An important distinction is the sense of the differential rotation of the mean flow – whether the steady mean flow is cyclonic or anti-cyclonic. We say that the flow is cyclonic (anti-cyclonic) at $r = \bar{r}$, for some constant \bar{r} , if the absolute value of the angular velocity Ω is an increasing (decreasing) function of r at $r = \bar{r}$. If Taylor–Couette flow is neither cyclonic nor anti-cyclonic, then it is either in solid-body rotation ($B = 0$, where, as shown later, no instabilities exist) or the mean velocity must be zero at $r = \bar{r}$ (hence (1) is satisfied for $r < \bar{r}$ and the flow is centrifugally unstable). Note that all flows satisfying (1) are anti-cyclonic.

By definition, the cyclonicity of the flow is determined by the sign of $(\Omega^2)'$ at $r = \bar{r}$. Multiplying by the positive term $\bar{r}/(2\Omega)^2$, we obtain a non-dimensional parameter,

$$S = \frac{\bar{r}\Omega(\bar{r})'}{2\Omega(\bar{r})} = \frac{-B}{A\bar{r}^2 + B}. \quad (26)$$

S is the ratio between the strain rate and twice the angular velocity, and we call it the relative strain rate. It can also be viewed as a Rossby number. In the framework of an environment rotating with angular velocity $\Omega(\bar{r})$, S is the ratio between the relative vorticity of the mean flow and the vorticity that is due to the rotating environment. In this context we recognize $|S| \ll 1$ as the well-known quasigeostrophic limit.

Based on these definitions we distinguish three different regimes for Taylor–Couette flow: 1. Anti-cyclonic, centrifugally unstable: Equation (1) is satisfied, $S < -1$, and A and B are of opposite signs.

2. Anti-cyclonic, centrifugally stable: Equation (1) is not satisfied, $-1 < S < 0$, and A and B have the same sign.

3. Cyclonic, centrifugally stable: Equation (1) is not satisfied, $S > 0$, and A and B are of opposite signs.

For example, when the outer cylinder is at rest, the flow is in the first regime. The limiting cases of $S = \pm\infty$ and $S = 0$ were discussed above. A third borderline case is $S = -1$, which corresponds to purely irrotational flow with $A = 0$. In our analysis we shall assume $S \notin \{-1, 0, \pm\infty\}$, although results can be obtained for the bounding cases by taking appropriate limits.

We choose $\bar{r} = (r_0 + r_1)/2$ to represent the characteristic length scale of the mean flow. The characteristic angular velocity is $\bar{\Omega} = \Omega(\bar{r})$, and the Froude number, $F = |\bar{\Omega}|/N$, represents the ratio between rotation and stratification. The non-dimensional gap width is denoted by $\epsilon = (r_1 - r_0)/\bar{r}$, and the non-dimensional angular velocity is given by $\tilde{\Omega} = \Omega/\bar{\Omega}$. The scaled azimuthal and vertical wavenumbers are given by

$$\tilde{\ell} = \epsilon\ell, \quad \tilde{m} = \epsilon m \bar{r} F. \quad (27)$$

The remaining non-dimensional values are $\tilde{r} = r/\bar{r}$, $y = \tilde{r}u/\bar{\Omega}\bar{r}$, and

$$\tilde{\sigma} = \frac{\sigma}{\tilde{\ell}\bar{\Omega}}, \quad \tilde{\omega} = \frac{\omega - \ell\bar{\Omega}}{\tilde{\ell}\bar{\Omega}}, \quad (28)$$

where we have subtracted the constant $\ell\bar{\Omega}$ from ω so that $\tilde{\omega}_r = 0$ will correspond to modes that are non-oscillatory in time relative to the mean flow at $r = \bar{r}$. Non-vanishing $\tilde{\ell}$ is assumed because we are investigating non-axisymmetric motions. Substitution into (25) yields

$$[\tilde{G}(1 - \tilde{\ell}^2\tilde{\sigma}^2F^2)\tilde{r}y']' + \left\{ \frac{2(S+1)}{\epsilon\tilde{\sigma}} [\tilde{G}(1 - \tilde{\ell}^2\tilde{\sigma}^2F^2)]' - \frac{4(S+1)\tilde{G}\tilde{\Omega}\tilde{r}\tilde{m}^2}{\epsilon^2} - \frac{\tilde{\ell}^2}{\epsilon^2\tilde{r}^2} \right\} y = 0, \quad (29)$$

with $\tilde{G} = (1 - \tilde{\ell}^2\tilde{\sigma}^2F^2 - \tilde{r}^2\tilde{m}^2\tilde{\sigma}^2)^{-1}$, where primes denote derivatives with respect to \tilde{r} .

3.4. Simplifications and analytical solutions

As we are unable to solve (29) analytically and generally, we make a regular perturbation analysis with respect to a small parameter $\tilde{\ell}^2$. That is, we assume that y can be expanded in a series of the form $y = y_0 + y_1\tilde{\ell}^2 + \dots$ and solve for y_0, y_1 , etc. Then, we compute the growth rate based on our approximate y . An important difference between this approach and the axisymmetric limit is that we can exploit the fact that $\tilde{\sigma}$ remains bounded as $\tilde{\ell} \rightarrow 0$ in the centrifugally stable regime. This allows us to obtain a relevant analytical, non-axisymmetric growth rate even in this limit.

3.4.1. Hydrostatic balance

To compute y_0 we must neglect all $\tilde{\ell}^2$ terms in (29). We do this in two steps. First we assume $\tilde{\ell}^2\tilde{\sigma}^2F^2 \ll 1$, and neglect only the $O(\tilde{\ell}^2F^2)$ terms. This is equivalent to the approximation of hydrostatic balance, often used in models of oceanic and atmospheric flow. This yields

$$(\tilde{G}_h\tilde{r}y')' + \left[\frac{2(S+1)}{\epsilon\tilde{\sigma}} \tilde{G}'_h - \frac{4(S+1)\tilde{G}_h\tilde{\Omega}\tilde{r}\tilde{m}^2}{\epsilon^2} - \frac{\tilde{\ell}^2}{\epsilon^2\tilde{r}^2} \right] y = 0, \quad (30)$$

with $\tilde{G}_h = (1 - \tilde{r}^2 \tilde{m}^2 \tilde{\sigma}^2)^{-1}$, where h subscripts denote that the hydrostatic assumption has been employed. Only a single term which includes the azimuthal wavenumber is left. If we neglect this term we obtain an equation whose two independent solutions can be written explicitly in terms of modified Bessel functions. These solutions are easier to obtain by first deriving a similar equation for v , as shown in Appendix B. However, to avoid subsequent complications, we prefer to simplify by employing a thin-gap approximation. In §5 we show numerically the weak influence of this simplification.

3.4.2. The thin-gap solution

We define a new non-dimensional independent variable, $x = (\tilde{r} - 1)/\epsilon$, which ranges from $-\frac{1}{2}$ (when $r = r_0$) to $\frac{1}{2}$ (when $r = r_1$). Substituting x into (30), we obtain in the thin-gap limit ($\epsilon \rightarrow 0$),

$$(\tilde{G}_{tg} y')' - [4(S + 1)\tilde{m}^2 \tilde{G}_{tg}(2S\tilde{G}_{tg} + 1) + \tilde{\ell}^2]y = 0, \quad (31)$$

where primes denote derivatives with respect to x . Here, $\tilde{G}_{tg} = (1 - \tilde{m}^2 \tilde{\sigma}_{tg}^2)^{-1}$ is the thin-gap limit of \tilde{G}_h , with $\tilde{\sigma}_{tg} = \lim_{\epsilon \rightarrow 0} \tilde{\sigma} = \tilde{\omega} - 2Sx$. In the small- $\tilde{\ell}$ limit (i.e. when the remaining $\tilde{\ell}^2$ term is neglected), the two independent solutions of (31) are given explicitly by

$$y = (1 + \alpha \tilde{\sigma}_{tg}) e^{-2\alpha x}, \quad (32)$$

where $\alpha = \pm \tilde{m} \sqrt{S + 1}$. (These are, as expected, the $\epsilon \rightarrow 0$ limits of the modified Bessel function solutions whose derivation is sketched in Appendix B.) Imposing the boundary conditions, $y(\pm \frac{1}{2}) = 0$, yields a quadratic equation for $\tilde{\omega}$ with solutions

$$\tilde{\omega} = \pm \frac{1}{\alpha} \sqrt{[\tanh(\alpha) + \alpha S][\coth(\alpha) + \alpha S]}. \quad (33)$$

Unstable modes occur when $\tilde{\omega}_i$ is positive. In the centrifugally stable regimes, $S > -1$, α is real, and the condition for instability is therefore

$$[\tanh(\alpha) + \alpha S][\coth(\alpha) + \alpha S] < 0. \quad (34)$$

For cyclonic flow, $S > 0$, (34) clearly cannot be satisfied by any real α , so no unstable modes exist in this limit. But for anti-cyclonic, centrifugally stable flow, $-1 < S < 0$, we can always choose \tilde{m} for which (34) is satisfied. In particular, the choice $\alpha S = \pm 1$ (i.e. $\tilde{m} = \pm 1/S \sqrt{S + 1}$), yields an unstable solution, because for any real α , $|\tanh(\alpha)| < 1 < |\coth(\alpha)|$. This solution is explicitly given by

$$\tilde{\omega}_i = -S \left(\frac{2e^{2/S}}{-\sinh(2/S)} \right)^{1/2} \approx -2Se^{2/S}. \quad (35)$$

Note that $\tilde{\omega}_i$ tends to zero exponentially fast as $S \rightarrow 0^-$. This implies that this instability is absent in the quasi-geostrophic approximation, defined as a regular perturbation expansion in S , as $|S| \rightarrow 0$.

The optimal- $\tilde{\omega}_i$ solution (i.e. $\tilde{\omega}_i$ which is maximal over \tilde{m} for a fixed S) is greater than the explicit solution of (35), but it tends to it exponentially as $S \rightarrow 0^-$. Similarly, the corresponding optimal \tilde{m} tends to $\pm 1/S \sqrt{S + 1}$ exponentially, and the range of \tilde{m} for which instabilities occur narrows exponentially. These results are shown in figure 1(a, b).

The eigenmodes corresponding to the unstable solutions are very smooth. Figure 1(c, d) shows the eigenmodes corresponding to (35) for $S = -0.5$, and -0.2 . The eigenmodes are normalized to be real at $x = 0$. The real part is then an even function

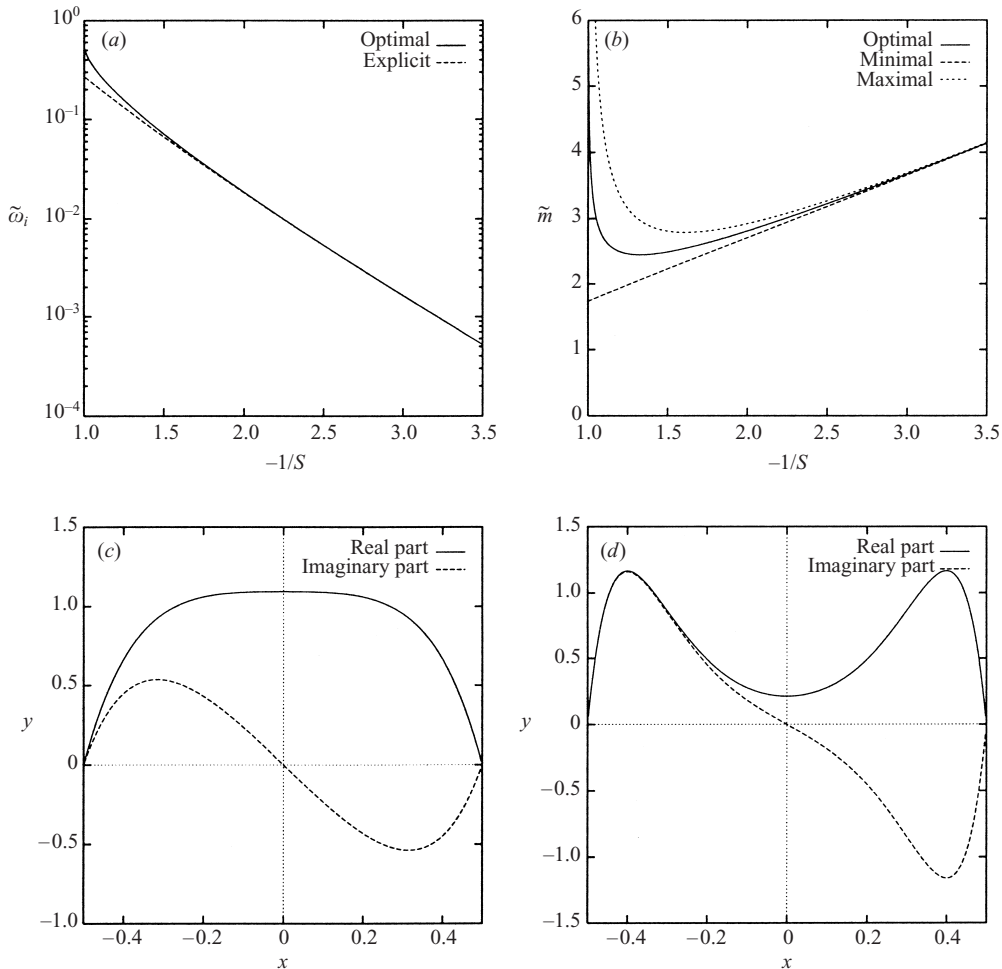


FIGURE 1. (a) The optimal $\tilde{\omega}_i$, in the limit of small $\tilde{\gamma}^2$ and thin gap, is compared to the explicit value of (35) for a range of S . (b) The optimal \tilde{m} is shown for a range of S . Also shown are the lower and upper limits of \tilde{m} for which unstable solutions exist. (c) Eigenmode, $y(x)$ for $S = -1/2$. (d) $y(x)$ for $S = -1/5$.

of x , and the imaginary part is an odd function. The eigenmodes become smoother for S closer to -1 . For $S \rightarrow 0^-$, the amplitude of the eigenmode concentrates in two ‘humps’ of width $O(|S|)$ near $x = \pm 0.5$, and there is an approximate 90° phase shift. That is, for $x \approx \frac{1}{2}$, $y(x) \approx -iy(-x)$. This structure, along with the other distinctive properties of the instability, is interpreted in §4.

3.4.3. An upper bound on ω_i

Equation (18) provides an upper bound on the growth rate ω_i . In the thin-gap limit we can identify the absolute value of the strain rate with $\|\mathcal{S}\|_\infty$. Noting that the growth rate of the (quadratic) perturbation energy is $2\omega_i$, we obtain from (26),

$$|\omega_i| \leq |\bar{\Omega}S|. \quad (36)$$

3.4.4. Implications of the analytic solution

We now summarize the main conclusions for the limit $\epsilon, \tilde{\ell} \rightarrow 0$ with moderate to strong stratification (F not large compared to 1):

(i) Unstable solutions exist for all anti-cyclonic flows ($S < 0$). This includes, of course, centrifugally unstable flows ($S < -1$, $AB < 0$; not addressed here) but also all flows for which $AB > 0$ (hence, $-1 < S < 0$). A sufficient condition for instability is thus $(d/dr)(V/r)^2 < 0$.

(ii) No unstable solutions exist in this limit for cyclonic flows with $S \geq 0$.

(iii) The growth rate, ω_i , is proportional to the scaled azimuthal wavenumber, $\tilde{\ell}$. But its main dependence is on the relative strain rate, S , and it decays exponentially fast as $|S|$ becomes small, $\omega_i \rightarrow -2S\bar{\Omega}\tilde{\ell} \exp(2/S)$ as $S \rightarrow 0^-$. This growth rate is $2\tilde{\ell} \exp(2/S)$ times the upper-bound value of (36).

(iv) Unstable solutions exist for a band of vertical wavenumbers which narrows exponentially fast as $S \rightarrow 0^-$ around $\tilde{m} = 1/S\sqrt{S+1}$. This implies that, in the limits $S \rightarrow -1$ (no rotation) and $S \rightarrow 0$ (pure rotation), the vertical scales of the unstable perturbations are very small compared to the radial scale, even after division by the Froude number. Away from these limits, the ratio of the vertical scale to the radial scale is $\sim F$ (which is also the most common aspect ratio for quasigeostrophic flows).

(v) The unstable eigenmodes are radially smooth—so indeed the gap width is an appropriate characteristic length scale for the perturbations—but they concentrate near the boundaries for $S \rightarrow 0^-$.

3.4.5. Higher-order approximation

The solution derived in §3.4.2 is only valid for small $\tilde{\ell}$. In order to obtain an analytical estimate of the optimal $\tilde{\ell}$ and the corresponding optimal growth rate, ω_i , we must compute the next-order solution in the small- $\tilde{\ell}$ expansion. Though far too complicated in general, for the hydrostatic equation (30) this tedious procedure (omitted for brevity) produces the following asymptotic estimate for the optimal ω_i in the limit of small $|S|$:

$$\omega_i^{asymptotic} \approx 2.03|\bar{\Omega}|\sqrt{-S}e^{2/S}, \quad S \rightarrow 0^-. \quad (37)$$

In figure 2 (§5) the asymptotic optimal growth rate of (37) is compared to the numerically computed value (obtained by optimizing ω_i over $\tilde{\ell}$ and \tilde{m}) for realistic parameters. It appears to provide a relevant approximation for the optimal growth rate despite the many simplifications. Furthermore, the numerical results show that near $S = -1$ the growth rate is about $0.315\bar{\Omega}$, that is, more than 30% of the upper-bound value (which by (36) is $|\bar{\Omega}|$). Hence, for a weak relative rotation rate, this instability is comparable in strength to centrifugal instabilities, although its strength decays exponentially for strong relative rotation rate.

3.5. Weak to moderate stratification

We now consider the case where F is not small compared to 1, and show that under certain assumptions the optimal growth rate tends to zero linearly with the stratification in the centrifugally stable regime (i.e. $\omega_i \propto 1/F$ as $F \rightarrow \infty$). This is consistent with the fact that no instabilities have been discovered in unstratified flows in this regime (Andereck *et al.* 1986; Tagg 1994). This relationship is also exhibited in our numerical computations.

In the weakly stratified regime, the relative azimuthal wavenumber is scaled

F	Vertical	Azimuthal	ω_i
0.015	0.027	3.148	0.12271
0.15	0.270	3.187	0.12172
1.5	3.019	6.353	0.07269
15.0	31.03	56.87	0.00882
150.0	310.6	568.0	0.00088

TABLE 1. Optimal growth rates and corresponding vertical and azimuthal wavelengths (measured in gap-width units) for $S = -2/3$, obtained numerically, with $\bar{r} = 1$ and $\epsilon = 0.1$.

differently than in (27). We denote it by $\check{\ell}$, defined by

$$\check{\ell} = \epsilon \ell F = \tilde{\ell} F. \quad (38)$$

With the remaining scaled variables unchanged, (29) becomes

$$[\check{G}(1 - \check{\ell}^2 \check{\sigma}^2) \check{r} y']' + \left\{ \frac{2(S+1)}{\epsilon \check{\sigma}} [\check{G}(1 - \check{\ell}^2 \check{\sigma}^2)]' - \frac{4(S+1) \check{G} \check{\Omega} \check{r} \check{m}^2}{\epsilon^2} - \frac{\check{\ell}^2}{\epsilon^2 \check{r}^2 F^2} \right\} y = 0. \quad (39)$$

Note that F appears only in the last term on the left-hand side of (39). Also, the small- $\check{\ell}^2$ solution holds for this regime as well in the limit $\check{\ell} \rightarrow 0$.

Recall that, by (28), (38), $\omega_i = \check{\ell} \check{\Omega} \check{\omega}_i / F$. It follows that if $\check{\ell} \check{\omega}_i$ is uniformly bounded as $F \rightarrow \infty$ then indeed the growth rate decays linearly with $1/F$. For any finite F and from (36), $\check{\ell} \check{\omega}_i$ is bounded, and, in the centrifugally stable regime, $\check{\omega}_i$ itself is bounded because $\omega_i \propto \check{\ell}$ as $\check{\ell} \rightarrow 0$. If these bounds are in fact independent of F , as $F \rightarrow \infty$, then the growth rate decays linearly with $1/F$ in this limit. Though we cannot be sure if this is indeed true, we point out that it can only be false if the last term on the left-hand side of (39) remains ‘important’ even as $F \rightarrow \infty$. The computational results in §5.2, plus the fact that no instabilities have been found for unstratified Taylor–Couette flows, suggest that this is not the case. Thus, stratification, usually found to be a stabilizing influence, is probably necessary for linear instability in this regime. Table 1 illustrates the dependence of the optimal growth rate, ω_i , and the perturbation wavelengths, measured in gap-width units, on F for $S = -2/3$. The optimal vertical wavelength is approximately proportional to F , with a slight transition near $F = 1$. The optimal growth rate and corresponding azimuthal wavelength are insensitive to F when F is small but approximately proportional to F when F is large. For large F the restriction that the wavelengths must equal the circumference divided by an integer precludes the large wavelengths required for optimal growth, unless ϵ is much smaller. The dependence of the growth rate on stratification is examined in greater detail in §5.2.

4. Interpretation

4.1. Rotating, stratified channel flow

Consider the flow between two parallel infinite planar walls, normal to the \bar{x} -axis of a Cartesian coordinate system, $(\bar{x}, \bar{y}, \bar{z})$, where \bar{z} denotes the vertical coordinate. Assume that the (viscous) flow is driven by an independent sliding of the walls in the

\bar{y} -direction. The mean flow is then given by $V = V(\bar{x})$, $U = W = 0$, where (U, V, W) denote the mean velocities in the $(\bar{x}, \bar{y}, \bar{z})$ directions, respectively, and $V(\bar{x})$ is linear and satisfies no-slip boundary conditions. Without loss of generality, $V = 0$ at the origin, located at the centre of the gap. Let d denote the gap width, and assume stable vertical density stratification, with constant N , and background rotation with angular velocity $\bar{\Omega}$ around a vertical axis. Assume perturbations of the form

$$(\hat{u}, \hat{v}, \hat{w}, \hat{p}, \hat{h}) = (u, v, w, p, h)(\bar{x}) e^{i(\ell\bar{y} + m\bar{z} - \omega t)}, \quad (40)$$

where w, p, h have the same meanings as before, but u, v are perturbations of the Cartesian velocities U, V . Let $\sigma = \omega - \ell V$, and introduce the scaling

$$\tilde{\omega} = \frac{\omega}{d\ell\bar{\Omega}}, \quad \tilde{\sigma} = \frac{\sigma}{d\ell\bar{\Omega}}, \quad \tilde{\ell} = d\ell, \quad \tilde{m} = dFm, \quad x = \frac{\bar{x}}{d}, \quad (41)$$

where $F = |\bar{\Omega}|/N$ is the Froude number, and the relative strain rate is $S = V'(\bar{x})/2\bar{\Omega}$. Then, beginning with the equations for the perturbations in the Cartesian coordinates and following a procedure analogous to that of Appendix A, we obtain the equation

$$[\tilde{G}(1 - \tilde{\ell}^2\tilde{\sigma}^2F^2)u']' + \left\{ \frac{2(S+1)}{\tilde{\sigma}} [\tilde{G}(1 - \tilde{\ell}^2\tilde{\sigma}^2F^2)]' - 4(S+1)\tilde{G}\tilde{m}^2 - \tilde{\ell}^2 \right\} u = 0, \quad (42)$$

with $\tilde{G} = (1 - \tilde{\ell}^2\tilde{\sigma}^2F^2 - \tilde{m}^2\tilde{\sigma}^2)^{-1}$, where primes denote derivatives with respect to x . Equation (42) is isomorphic to the thin-gap equation for linear perturbations around Taylor–Couette flow; if we now use the hydrostatic approximation to neglect $O(\tilde{\ell}^2F^2)$ terms, we obtain (31).

A similar exercise shows that the analogue of this problem for a thin, uniform-density layer (i.e. the shallow-water equations) version of this problem also yields an isomorphism. However, because \tilde{m} is no longer a freely chosen wavenumber, the instability occurs only for a particular narrow range of layer thickness and a given S . This problem, albeit in a non-rotating environment ($S = -1$), is studied theoretically and numerically by Satomura (1981a, 1982). He observes instabilities for a sufficiently large Froude number, which he interprets as unstable shear-modified gravity waves.

4.2. Kelvin-wave coupling

The instability described here has several distinctive properties, some of which are further demonstrated in §5. It requires stratification; it occurs only for anti-cyclonic flow; the growth rate decays as an exponential function of $2/S$; in the hydrostatic limit it only occurs for a narrow band of vertical wavenumbers, although it is not very sensitive to variations in the azimuthal wavenumber; it is quite insensitive to the gap width; and the eigenfunctions are usually smooth, but for small $|S|$ they concentrate in two ‘humps’ near the boundaries, which are phase-shifted by nearly 90° relative to each other.

The underlying mechanism of this instability is described in Kushner *et al.* (1998) for the uniform-shear channel-flow problem. It is interpreted as an interaction between two shear-modified Kelvin waves which are held in place by the mean flow. Since the non-centrifugal Taylor–Couette instability is approximated well by the channel-flow equation even for moderate gap width (§5), it is evident that the same mechanism applies to Taylor–Couette flow. Indeed, this interpretation explains all the important features of the instability: (a) Kelvin waves can only occur in the presence of stratification; (b) anti-cyclonic shear is required to arrest the waves, since they propagate cyclonically; (c) the given steady shear dictates a particular phase speed for the Kelvin waves that would allow their arrest, which in turn implies a particular vertical

wavenumber; and (d) the energy perturbation growth occurs as a result of the u, v correlation between Kelvin waves at opposite boundaries, as implied by (16). This explains the 90° phase shift and the exponential decay of the growth rate.

Similar cases of ageostrophic instabilities due to resonance of waves have been observed and reported in the literature previously. Satomura (1981*a, b*) finds qualitatively similar behaviour for shallow-water shear flow that is unbounded or bounded only on one side (with piecewise-linear mean velocity profiles). Griffiths, Killworth & Stern (1982) study shallow-water gravity currents whose depth vanishes on both sides of the flow. They demonstrate ageostrophic instabilities by a linear stability analysis and laboratory experiments. Hayashi & Young (1987) analyse a similar problem with varying rotation (β -plane) in the framework of a study on energy and momentum transfer to and from unstable waves. They interpret the instabilities as a resonance of shear-modified Kelvin and gravity waves. A similar view of instabilities due to the interaction of waves and shear is given by Sakai (1989).

5. Computational results

Now we present results from computational solutions of the linear stability problem in order to test the effects of a finite gap width, the restriction of the azimuthal wavenumbers to integers, the dependence on the Froude number, and a finite viscosity. Further, we find that there are many more unstable modes (probably infinitely many), with countable radial ‘modenumbers’, in the case where the stratification is strong and the azimuthal wavenumbers are not small (hence undetectable by the small- $\tilde{\ell}$ analysis in §3.4). The numerical solver is based on a straightforward second-order-accurate, finite-volume discretization of (25). For given physical parameters and wavenumbers ℓ and m , we search for eigenfrequencies ω for which the matrix representing the discretized equation is singular. We do this by computing for a uniform $(\tilde{\omega}_r, \tilde{\omega}_i)$ grid the smallest (in absolute value) eigenvalues of the matrices, obtained by an inverse power method. We then plot colour-maps of the results and (literally) look for local ‘lows’. Once the vicinity of a singularity is thus spotted, we use a standard minimization technique to home in on the precise eigenfrequency. Once an instability is found, we can easily track it automatically as we slowly vary parameters.

The numerical computations in the viscous case were performed using the code of Molemaker & Dijkstra (2000), who employ finite differences in the radial and vertical directions and use an Arnoldi method for finding the most unstable modes. The results of the two codes matched extremely well in inviscid comparisons.

5.1. Finite gap width, finite stratification, integer ℓ

We first test the effects of the thin-gap approximation and of the hydrostatic assumption. The growth rate, optimized with respect to ℓ and m , is computed for $\epsilon = 0.1, 0.2,$ and 0.3 , with $\bar{r} = 1$, and plotted for a range of S values and compared with the thin-gap hydrostatic solution of (31) (denoted $\epsilon = 0$) in figure 2. We fix the stratification N and the irrotational part of the flow, $B = 1$, and vary S by varying the rotation rate, A . (As a result the Froude number varies proportionally to $-1/S$. We use its value at $S = -1$ as the reference value.) For the results shown in figure 2, F is 0.1 , which implies strong stratification (yet much weaker than is typical for large-scale oceanic flows).

It is evident from figure 2 that, even for only moderately strong stratification, the optimal growth rate is approximated very well by the hydrostatic equation. Furthermore, the dependence on the finite gap width is quite weak, even for $\epsilon = 0.3$,

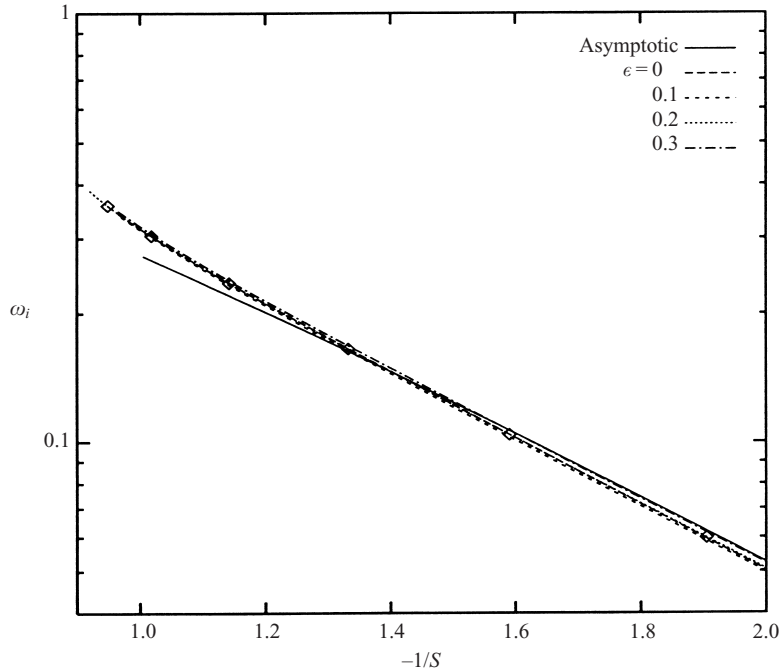


FIGURE 2. Optimal growth rate, ω_i , for a range of S and several values of relative gap width, ϵ (including the thin-gap limit denoted $\epsilon = 0$). The nominal F is 0.1, except the thin-gap result which is hydrostatic. The symbols indicate where the optimal ℓ of the $\epsilon = 0.2$ solution is an integer. Here, $B, \bar{r} = 1$. The solid line shows the approximate asymptotic growth rate of (37).

which corresponds to a wider gap than that of the experiments of Boubnov *et al.* (1995). The symbols in the plot show where the optimal ℓ is an integer (ranging from 6 to 11) for the case $\epsilon = 0.2$. In fact, the dependence of the growth rate on ℓ (for optimal m) is so weak that, if we restrict ℓ to integer values, the change in figure 2 would be imperceptible. Note, by the way, that the instabilities vary smoothly as we pass into the centrifugally unstable regime, $S < -1$.

5.2. Dependence on stratification

Next, we test our scaling estimate for the dependence of the optimal growth rate, ω_i , on the Froude number. Figure 3 shows the optimal ω_i vs. F for $S = -19/20$ and $S = -2/3$. Clearly, the growth rate varies essentially linearly with $1/F$ when F is large compared to 1, but it is almost independent of F when the Froude number is small. The azimuthal wavenumber behaves in a similar way, as predicted.

5.3. Large- $\tilde{\ell}$ instabilities

In addition to the coupled Kelvin-wave instability, our numerical computations reveal another family of instabilities with distinct characteristics. They exist only when the stratification is strong and the scaled azimuthal wavenumber, $\tilde{\ell}$, is not too small. Indeed, the small- $\tilde{\ell}$ analysis implies that the Kelvin-wave instability described above is the only unstable solution for $\tilde{\ell} \rightarrow 0$. So we call the newly found modes ‘large- $\tilde{\ell}$ instabilities’.

This family of instabilities has many members, probably infinitely many, characterized by integer radial ‘mode numbers’ associated with the shape of the eigenmode

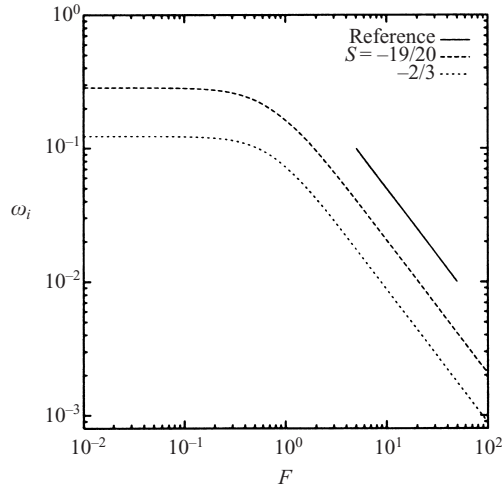


FIGURE 3. Optimal growth rate, ω_i , vs. the Froude number for two values of S . The solid line, provided for reference, is proportional to $1/F$.

as shown below. We use k to denote the mode number, with, for convenience, $k = 0$ denoting the small- $\tilde{\ell}$ (Kelvin-wave) instability mode. For the $k > 0$ modes, $\omega_r \neq 0$, but they are nevertheless non-oscillatory in time with respect to some point (which depends on k) that is still within the gap. Figure 4(a) shows the optimal ω_i for the first five modes and also, for comparison, for the $k = 0$ mode, all using the thin-domain, hydrostatic equation. (We verified that, here too, the dependence on a finite gap width and finite F is weak, albeit not as weak as for the small- $\tilde{\ell}$ instability.) Though still substantial, the growth rates are weaker for the large- $\tilde{\ell}$ family. Furthermore, the decay rate of ω_i with decreasing $|S|$ is exponentially faster. This is quantified in figure 4(b), which shows that the optimal growth rates appear to satisfy an approximate asymptotic formula of the form

$$\omega_i^{asymptotic} \sim |\bar{\Omega}|k^{-1/4}e^{3/S}, \quad k > 0. \quad (43)$$

Figure 4(b) shows the optimal growth rates divided by the empirical asymptotic formula (43) for the first five high- $\tilde{\ell}$ modes. Also, we computed the first 22 modes for $S = -2/3$, and the corresponding values are highlighted in figure 4(b) to show the validity of the $k^{-1/4}$ asymptotic approximation.

Figure 4(c,d) shows the third and fifth optimal-growth large- $\tilde{\ell}$ eigenmodes for $S = -2/3$, normalized such that the real and imaginary parts are highly correlated in the right-hand region.† The mode number is determined by the number of extrema in the correlated part. We computed the first 22 modes. No doubt, there are infinitely many such modes, consistent with the conclusion of Satomura (1981a) and the large- ℓ matched asymptotics solution of Knessl & Keller (1992) to the related problem of Griffiths *et al.* (1982). We found that $\tilde{\ell}^2, \tilde{m}^2$, grow approximately linearly with k , and $\tilde{\ell}^2/\tilde{m}^2$ is nearly independent of k . These behaviours can be understood by rewriting (31) for a new dependent variable, $z = \tilde{m}\tilde{\sigma}_{tg} = -2\tilde{m}Sx$. The equation depends only on $\tilde{\ell}^2/\tilde{m}^2$, not on each of the wavenumbers separately. The dependence on \tilde{m} enters only

† Because of reflection symmetry about $x = 0$ in the thin-gap limit, the modes are pairwise degenerate such that $\omega_r \rightarrow -\omega_r$ and $y(x) \rightarrow y(-x)$ is also a mode.

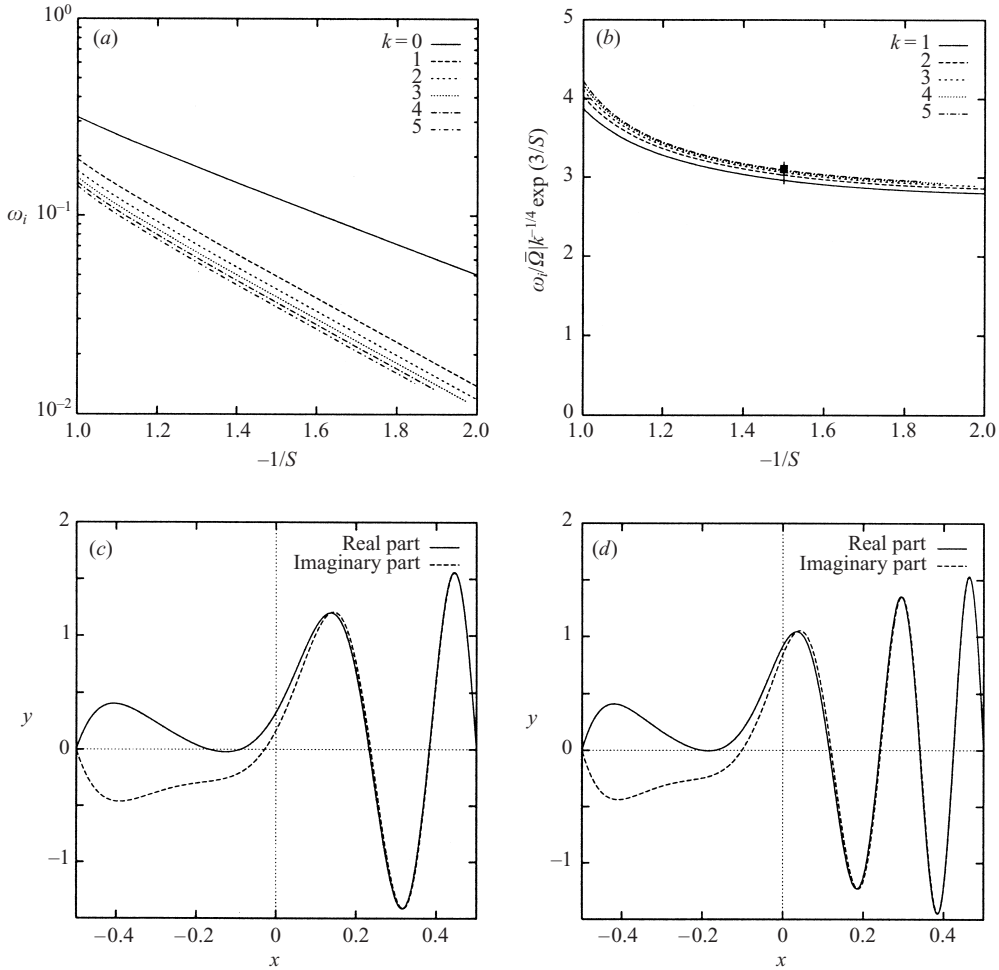


FIGURE 4. (a) Optimal growth rate, ω_i , for the first five large- $\tilde{\ell}$ modes, compared to the small- $\tilde{\ell}$ mode (denoted $k = 0$) for a range of S . (b) Optimal ω_i for the first five high- $\tilde{\ell}$ modes, divided by $|\tilde{\Omega}|k^{-1/4} \exp^{3/S}$. The points marked by + signs show the values corresponding to the first 22 modes at $S = -2/3$. (c) Eigenmode $k = 3$. (d) Eigenmode $k = 5$.

through the boundary conditions and has an extremely weak effect on the optimal wavenumber ratio. A WKB analysis shows that for large k we must have $k^2 \sim \tilde{\ell}^2 \tilde{m}^2$. The main conclusion we draw from these computations is that the optimal ω_i appears to decay like $k^{-1/4}$ for large k , as shown in figure 4(b).

Although we do not have a simple explanation for the dynamical mechanism of the large- $\tilde{\ell}$ instability, there are two strong indications that it is similar in nature to the $k = 0$ mode: the exponential dependence of the growth rate on $3/S$ and the fact that, if y is nearly real near one boundary, then it is nearly imaginary near the other, as suggested by figure 4(c, d). Considering (31), we speculate that in parts of the domain where \tilde{G}_{tg} is negative and sufficiently small (particularly near the boundary), $\tilde{\ell}$ dominates in the second term, and the solution is a modified inertial–gravity wave. But where \tilde{G}_{tg} is large we again obtain a shear-modified Kelvin wave. The overall solution is a combination of the two regimes.

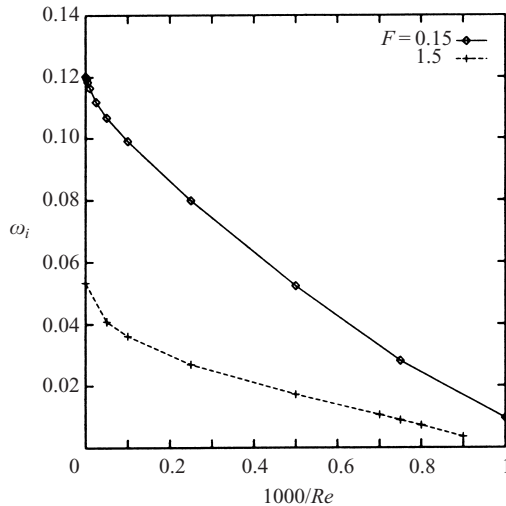


FIGURE 5. Optimal growth rates vs. the Reynolds number for $S = -2/3$, $\epsilon = 0.1$.

5.4. Viscous effects

We test the robustness of our linear stability results to a finite viscosity. In particular, we wish to verify that the instabilities persist when no-slip boundary conditions are imposed. Using the code of Molemaker & Dijkstra (2000), we compute solutions for the $k = 0$ instability with $\epsilon = 0.1$, $\bar{r} = 1$, $B = 2A = 1$ (i.e. $S = -2/3$), with strong and moderate stratification, $N = 10$ and 1 ($F = 0.15$ and 1.5), respectively. We use a grid of 256 mesh points in the radial direction to resolve the boundary layers.

To facilitate comparisons to plane Couette flow (e.g. Bech & Andersson 1997) we define the Reynolds number by

$$Re = \frac{|\mathcal{L}|[0.5(r_1 - r_0)]^2}{\nu} = \frac{|S\bar{\Omega}|\bar{r}^2\epsilon^2}{2\nu}. \quad (44)$$

We find that the flow is linearly unstable for Re greater than about 1000. The dependence of the optimal growth rate on Re is shown in figure 5. The viscous eigenmodes, shown in figure 6, are very similar to the inviscid ones, except in boundary layers near the walls that become increasingly thin with Re .

6. Nonlinear evolution

The importance of the linear instability for the nonlinear dynamics of the flow at supercritical values of Re needs to be tested. Even in the absence of linear instabilities, it is expected that at sufficiently high Reynolds numbers Taylor–Couette flow undergoes a transition to turbulence. Therefore, it is possible that the linear instability could be obscured by finite-amplitude perturbation growth.

To investigate the relevance of the linear instability in the supercritical regime, we integrate numerically the three-dimensional, nonlinear, time-dependent, viscous Boussinesq equations (4) to examine the nonlinear equilibration of the linear instability. The main results are summarized here, but a more complete report is in Molemaker, McWilliams & Yavneh (2001). The computations are performed for a strongly stratified, narrow-gap regime at $S = -2/3$.

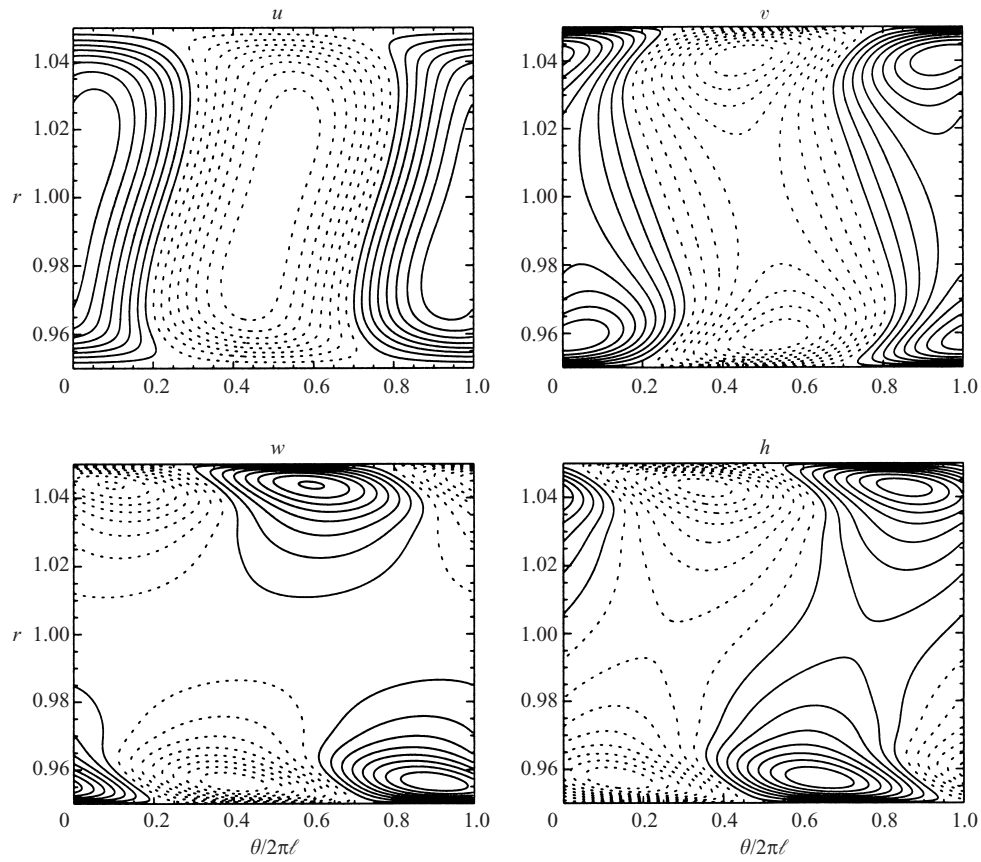


FIGURE 6. Contour plots of a viscous solution with $S = -2/3$, $F = 1.5$.

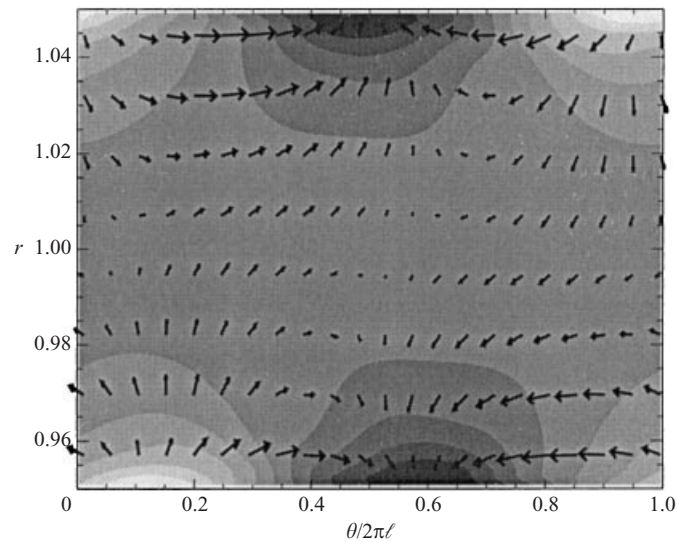


FIGURE 7. A horizontal cross-section of the nonlinear equilibrated flow is shown for $Re \approx 4000$. Horizontal velocities are shown as vectors, and vertical velocities are shown by grey-level, where lighter/darker shades represent upward/downward motions.

At the critical value of $Re \approx 1120$ (somewhat higher than indicated in figure 5 due to a finite diffusivity for density), the flow undergoes a supercritical pitchfork bifurcation. A stationary, nonlinear solution is obtained which is stable for a significant range of Re . In figure 7 such a solution is shown for $Re \approx 4000$. Despite the strong nonlinearity of this solution, it clearly resembles the linear eigenmode such as shown in figure 6. It is distorted somewhat by nonlinear effects, most notably changing the phase difference between upper and lower boundary Kelvin waves. At a slightly higher Re , the stationary solution is destabilized by an oscillatory perturbation corresponding to a supercritical Hopf bifurcation. The resulting stable limit cycle is very clearly driven by the linear instability dynamics. Subsequent bifurcations eventually lead to fully developed turbulent flow.

This scenario is radically different from that of cyclonic mean flow, where, in the absence of linear instabilities, fluctuation growth occurs by finite-amplitude mechanisms, and the transition to turbulent flow is much more abrupt. Our computations indicate that no such transition occurs in the range of Reynolds numbers for which the linear instability dominates the dynamics of anti-cyclonic flow. These results show that in realizable laboratory conditions the linear instability plays an essential role in the dynamics of Taylor Couette flow.

7. Conclusions

We have investigated the flow between two concentric cylinders in a fluid with stable axial stratification that does not satisfy the Rayleigh condition for axisymmetric instability. For such flows no instabilities are believed to exist in the classical (unstratified) Taylor–Couette flow. However, we find from both a linear stability analysis and nonlinear integrations that all anti-cyclonic flows are linearly unstable for sufficiently high Reynolds numbers. Thus, a sufficient condition for linear instability is $d(V/r)^2/dr < 0$, which implies a far wider regime of instability than previously identified. The growth rates of the fastest growing mode are strong (over 30% of the upper bound) when the relative strain rate (Rossby number), S , is close to -1 , but they decay as an exponential function of $2/S$ as $S \rightarrow 0^-$. This is indicated by analytical solutions obtained for flows whose azimuthal wavelengths are larger than the gap width, and by numerical computations for a wide range of parameters. The instability depends crucially on the stratification. The growth rate is essentially proportional to the stratification when the latter is weak (Froude numbers F large compared to 1), but it is independent of the stratification for small F . Strong instabilities only occur for a particular narrow band of vertical wavenumbers, but they are relatively insensitive to variations in the azimuthal wavenumber and quite insensitive to changes in the gap width. The instability is analogous to that found in uniform shear flow of a stratified fluid in a rotating channel, as analysed and interpreted as an interaction between shear-modified Kelvin waves by Kushner *et al.* (1998).

The radial length scale of the fastest-growing modes is the gap width, d . For small F the azimuthal length scale is $\sim d$, but the vertical length scale is $\sim Fd$, i.e. similar to the so-called Prandtl scaling that commonly occurs in quasi-geostrophic flows. For large F both the vertical and azimuthal scales are $\sim Fd$.

Although all the analytical results are obtained in the inviscid limit, we also compute viscous solutions. We find that the instabilities persist in the presence of a sufficiently small viscosity, and we show the dependence of the optimal growth rate on the Reynolds number. Furthermore, nonlinear three-dimensional initial-value

computations demonstrate unambiguously the central role of the linear instability in the nonlinear dynamics of stratified, centrifugally stable Taylor–Couette flow (see also Molemaker *et al.* 2001).

The instability analysed here is of a mostly unfamiliar type for laboratory and geophysical fluid dynamicists, being neither barotropic, nor baroclinic, nor centrifugal/inertial, nor convective. It has potentially great geophysical relevance in the regime of intermediate Rossby and Froude numbers that characterize flows that occur on intermediate scales (i.e. the mesoscales) between anisotropic, geostrophic, large-scale motions and isotropic, unbalanced, small-scale motions. However, much remains to be learned about this regime before its relevance can be fully assessed. For example, how does the instability change for more general velocity shear profiles? How essential to its occurrence is the presence of horizontal boundaries? How is it related, if at all, to the elliptical instability of an unbounded flow with uniform vorticity and strain rate at intermediate Rossby and Froude numbers (Miyazaki 1993; McWilliams & Yavneh 1998)? How relevant is it to the breakdown of balanced flows and their fully developed turbulence?

We thank Phil Marcus for his advice and Noa Porrat for her help in the early stages of this work. Part of this work was carried out by the first two authors while visiting the National Center for Atmospheric Research. Support was also provided by the Office of Naval Research through grant # ONR N00014-98-1-0165, by The Technion V. P. R. Fund for the Promotion of Sponsored Research, and by The Fund for the Promotion of Research at the Technion.

Appendix A. Derivation of equation for u

To derive a single equation for the radial velocity perturbation, u , we first eliminate h from (22), (23), obtaining

$$w = -\frac{m\sigma p}{N^2 - \sigma^2}. \quad (\text{A } 1)$$

Next we eliminate w from (24), (A 1), obtaining

$$p = -i \left[\frac{1}{r}(ru)' + \frac{i\ell}{r}v \right] \frac{N^2 - \sigma^2}{m^2\sigma}. \quad (\text{A } 2)$$

Substitution of (A 2) into (21) and isolation of v produces

$$v = iG[\ell(N^2 - \sigma^2)(ru)' + \sigma m^2 Z r^2 u], \quad (\text{A } 3)$$

with $G = [\ell^2(N^2 - \sigma^2) - r^2 m^2 \sigma^2]^{-1}$. Finally, we use (A 2) and (A 3) to eliminate p and v from (20). Dividing through by i and using (15), we obtain after simple manipulation (first substituting (A 3) into (A 2))

$$\begin{aligned} & [G(N^2 - \sigma^2)\sigma r(ru)']' + G\ell(N^2 - \sigma^2)r\Omega'(ru)' \\ & + \left\{ \ell[G(N^2 - \sigma^2)Z]' - 2G\Omega Z r m^2 \sigma - \frac{\sigma}{r} \right\} (ru) = 0. \quad (\text{A } 4) \end{aligned}$$

We simplify (A 4) slightly by using $\sigma' = -\ell\Omega'$ to combine the first and second terms. Dividing through by σ we thus obtain (25).

Appendix B. Equation for v and the small- $\tilde{\ell}$ solution

To derive an equation for the azimuthal velocity perturbation, v , we first eliminate u from (20), (21), obtaining

$$(\sigma^2 - 2\Omega Z)v + Zp' - \frac{\sigma \ell p}{r} = 0. \quad (\text{B } 1)$$

Eliminating u from (21), (B 1), using the fact that Z is constant, yields

$$\frac{\ell Z v}{r} + \frac{(r\sigma v)'}{r} - \frac{m^2 \sigma Z p}{N^2 - \sigma^2} - \frac{\ell p'}{r} = 0. \quad (\text{B } 2)$$

Eliminating p' from (B 1), (B 2) yields

$$\frac{\ell[\sigma^2 + Z(Z - 2\Omega)]v}{r} + \frac{Z(r\sigma v)'}{r} - \left(\frac{\ell^2}{r^2} + \frac{m^2 Z^2}{N^2 - \sigma^2} \right) \sigma p = 0, \quad (\text{B } 3)$$

which can be simplified, using (15) and $\sigma' = -\ell\Omega'$, to produce (after division by σ)

$$\frac{\ell \sigma v}{r} + \frac{Z(rv)'}{r} - \left(\frac{\ell^2}{r^2} + \frac{m^2 Z^2}{N^2 - \sigma^2} \right) p = 0. \quad (\text{B } 4)$$

Isolating p in (B 4) and substituting into (B 1) yields

$$[KrZ^2(N^2 - \sigma^2)(rv)']' + \{r[KZ\ell\sigma(N^2 - \sigma^2)]' - K\ell^2\sigma^2(N^2 - \sigma^2) + (\sigma^2 - 2\Omega Z)\} v = 0, \quad (\text{B } 5)$$

with $K = [\ell^2(N^2 - \sigma^2) + m^2 r^2 Z^2]^{-1}$. We next non-dimensionalize (B 5) and neglect $O(\tilde{\ell}^2)$ terms. Multiplying by $\tilde{m}^2/\epsilon^2\tilde{\Omega}^2$ we obtain

$$v'' + \frac{v'}{\tilde{r}} - \left(\beta^2 + \frac{\mu^2}{\tilde{r}^2} \right) v = 0, \quad (\text{B } 6)$$

where primes denote derivatives with respect to \tilde{r} and

$$\beta = \frac{2\tilde{m}(S+1)}{\epsilon}, \quad \mu = \sqrt{1 - \frac{4\tilde{m}^2 S(S+1)}{\epsilon^2}}. \quad (\text{B } 7)$$

The two independent solutions to (B 6) are

$$v = I_{\pm\mu}(\beta\tilde{r}), \quad (\text{B } 8)$$

where I is the modified Bessel function. From (B 8) we can easily obtain the small- $\tilde{\ell}$ solutions of p , and then u , using the scaled form of (B 4) (neglecting $O(\tilde{\ell}^2)$ terms) and (21).

REFERENCES

- ANDERECK, C. D., LIU, S. S. & SWINNEY, H. L. 1986 Flow regime in a circular Couette system with independently rotating cylinders. *J. Fluid Mech.* **164**, 155–183.
- BECK, K. H. & ANDERSSON, H. I. 1997 Turbulent plane Couette flow subject to strong system rotation. *J. Fluid Mech.* **347**, 289–314.
- BOUBNOV, B. M., GLEDZER, E. B. & HOPFINGER, E. J. 1995 Stratified circular Couette flow: instability and flow regimes. *J. Fluid Mech.* **292**, 333–358.
- BOUBNOV, B. M., GLEDZER, E. B., HOPFINGER, E. J. & ORLANDI, P. 1996 Layer formation and transition in stratified circular Couette flow. *Dyn. Atmos. Ocean* **23**, 139–154.
- BOUBNOV, B. M. & HOPFINGER, E. J. 1997 Experimental study of circular Couette flow in a stratified fluid. *Fluid Dyn.* **32**, 520–528.

- CATON, F., JANIAUD, B. & HOPFINGER, E. J. 1999 Primary and secondary Hopf bifurcations in stratified Taylor–Couette flow. *Phys. Rev. Lett.* **82**, 4647–4650.
- CHANDRASEKHAR, S. 1961 *Hydrodynamic and Hydromagnetic Stability*. Oxford University Press.
- COUETTE, M. 1890 Etudes sur le frottement des liquides. *Ann. Chim. Phys.* **21**, 433–510.
- GRIFFITHS, R. W., KILLWORTH, P. D. & STERN, M. E. 1982 Ageostrophic instability of ocean currents. *J. Fluid Mech.* **117**, 343–377.
- HAYASHI, Y.-Y. & YOUNG, W. R. 1987 Stable and unstable shear modes of rotating parallel flows in shallow water. *J. Fluid Mech.* **184**, 477–504.
- HUA, B. L., LE GENTIL, S. & ORLANDI, P. 1997 First transitions in circular Couette flow with axial stratification. *Phys. Fluids* **9**, 365–375.
- HUA, B. L. & MOORE, D. W. 1994 Inertial instability of subthermocline equatorial flows. *Annales Geophysicae* **12**(Suppl.), C221.
- KNESSL, C. & KELLER, J. B. 1992 Stability of rotating shear flows in shallow water. *J. Fluid Mech.* **244**, 605–614.
- KUSHNER, P. J., MCINTYRE, M. E. & SHEPHERD, T. G. 1998 Coupled Kelvin-wave and mirage-wave instabilities in semigeostrophic dynamics. *J. Phys. Oceanogr.* **28**, 513–518.
- MCWILLIAMS, J. C. & YAVNEH, I. 1998 Fluctuation growth and instability associated with a singularity of the Balance Equations. *Phys. Fluids* **10**, 2587–2596.
- MCWILLIAMS, J. C., YAVNEH, I., CULLEN, M. J. P. & GENT, P. R. 1998 The breakdown of large-scale flows in rotating, stratified fluids. *J. Phy. Fluids* **10**, 3178–3184.
- MIYAZAKI, T. 1993 Elliptical instability in a stably stratified rotating fluid. *Phys. Fluids A* **5** 2702–2709.
- MOLEMAKER, M. J. & DIJKSTRA, H. A. 2000 Stability of a cold core eddy in the presence of convection: Hydrostatic versus non-hydrostatic modeling. *J. Phys. Oceanogr.* **30**, 475–494.
- MOLEMAKER, M. J., MCWILLIAMS, J. C. & YAVNEH, I. 2001 Instability and equilibration of centrifugally-stable stratified Taylor–Couette flow. *Phys. Rev. Lett.* **86**, 5270–5273.
- OYAMA, K. 1966 On the stability of the baroclinic circular vortex: a sufficient condition for instability. *J. Atmos. Sci.* **23**, 43–53.
- RAYLEIGH, LORD 1916 On the dynamics of revolving fluids. *Proc. R. Soc. Lond. A* **93**, 148–154.
- SAKAI, S. 1989 Rossby-Kelvin instability: a new type of ageostrophic instability caused by a resonance between Rossby waves and gravity waves. *J. Fluid Mech.* **202**, 149–176.
- SATOMURA, T. 1981a An investigation of shear instability in a shallow water. *J. Met. Soc. Japan* **59**, 148–167.
- SATOMURA, T. 1981b Supplementary note on shear instability in a shallow water. *J. Met. Soc. Japan* **59**, 168–171.
- SATOMURA, T. 1982 An investigation of shear instability in a shallow water, part II: numerical experiment. *J. Met. Soc. Japan* **60**, 227–244.
- TAGG, R. 1994 The Couette–Taylor problem. *Nonlin. Sci. Today* **4**, 1–25.
- TAYLOR, G. I. 1923 Stability of a viscous fluid contained between two rotating cylinders. *Phil. Trans. R. Soc. Lond. A* **233**, 289–343.
- THORPE, S. A. 1966 The stability of stratified Couette flow. *Notes on 1966 Summer School on Geophys. Fluid Dyn.*, pp. 80–107, Woods Hole Oceanographic Inst.